applied sciences

MDPI

Article

The Modularized Development of a Wheel-Side Electric Drive System Using the Process of Hobbing and Form Grinding

Xiaoyu Ding [1,2], Wei Wang [3] and Xinbo Chen [2,*]

[1] R&D Innovation Headquarters, SAIC Motor, Shanghai 201804, China; dingxiaoyu@tongji.edu.cn
[2] School of Automotives Studies, Tongji University, Shanghai 201804, China
[3] Department of Mechanical Systems Engineering, Tokyo University of Agriculture and Technology, Tokyo 184-8588, Japan; weiwang@go.tuat.ac.jp
* Correspondence: chenxinbo@tongji.edu.cn

Abstract: The wheel-side electric drive system is a melding of a vehicle powertrain and suspension system, which saves chassis space and can adapt to different models. To achieve the goal of highly modularized development, the system is supposed to meet the requirements of various working conditions without changing the interface state. The electric motor drives the wheel through two-stage fixed axis helical gears, so the transmission is short in path and acts as the suspension arm at the same time. As a result, the gears are critical to output robustness and NVH performance. The modeling accuracy is decisive for simulations and tests, so it is necessary to build a precise geometric model instead of the data-fitting estimation. The gears are manufactured by a hobbing and form grinding process, which is described functionally along with the relationship between the tooling parameters and tooth profile curves. Based on the rain flow methodology and extrapolation theory, a comprehensive load spectrum with nine stages is formulated, which can cover the working conditions of a basic version, a NVH version, and a durability version. According to the Miner cumulative damage hypothesis, the equivalent durability mileage of 150,000 km is converted. The prototype machine is simulated and verified on the test bench, and the test results show that the wheel-side electric drive system has a reliable output performance. The equivalent damage of the comprehensive load spectrum is 63.27%, where the 2# stage driving gear is the most vulnerable component of the whole system. The research in this paper can provide data support for damage calculation and lightweight optimization with modularized development and applications in the future.

Keywords: wheel-side electric drive system; hobbing and form grinding; load spectrum; durability test

check for updates

Academic Editor: Francesco Liberato Cappiello

Received: 1 January 2025
Revised: 27 January 2025
Accepted: 30 January 2025
Published: 31 January 2025

Citation: Ding, X.; Wang, W.; Chen, X. The Modularized Development of a Wheel-Side Electric Drive System Using the Process of Hobbing and Form Grinding. *Appl. Sci.* **2025**, *15*, 1483. https://doi.org/10.3390/app15031483

Copyright: © 2025 by the authors. Licensee MDPI, Basel, Switzerland. This article is an open access article distributed under the terms and conditions of the Creative Commons Attribution (CC BY) license (https://creativecommons.org/licenses/by/4.0/).

1. Introduction

In recent years, distributed electric drive technology has developed rapidly. The independent control of each wheel can be achieved, thus improving the off-road performance and maneuverability of the vehicle [1]. However, the distributed electric drive technology usually increases the unsprung mass of vehicle suspension, which has a negative impact on riding comfort and handling stability [2]. In addition, the distributed drive system works in the environment with continuous vibration and impact, which poses a significant challenge to the reliability of the system [3]. In the patent [4], the author's research team proposed a wheel-side electric drive system with a motor and two-stage fixed axis helical gears. It transfers the motor position from inside the wheel to the wheel-side space, which reduces the equivalent unsprung mass of the traditional in-wheel motor. The wheel-side

electric drive system works as a trailing arm suspension at the same time, which is characterized with high compactness [5]. From the perspective of automotive engineering, the wheel-side electric drive system is a melding of a vehicle powertrain and suspension system [6]. Initially a design concept, and it is now supposed to be equipped on a chassis for different models, such as a sedan, off-road vehicle, tourist sightseeing car, or golf cart. The working condition significantly varies, while the system is expected to meet the customized requirements without changing the interface state. Thus, the benefits of interchangeability and circular-use brought by modularization can be fully achieved.

Currently, the development and industrialization of an electric drive system usually focuses on a specific vehicle model and its working conditions [7], conducting a bench test with the corresponding load spectrum to evaluate the durability performance, NVH performance, system energy consumption, etc. A single bench test like this needs more than 500 h to complete, and during the development of a single vehicle model, it is necessary to perform three bench tests for the electric drive system to ensure the reliability with sufficient sample numbers [8]. However, for the modularized wheel-side electric drive system, it is almost impossible to develop and test for the vehicle model case by case. For example, if the wheel-side electric drive system is applied in three models with different working conditions, then the bench test will take over 4500 h, which is totally unacceptable in terms of time cost and financial expense. As a result, it is necessary to study the equivalent conversion of load spectrum to improve the development efficiency. There is existing research in this area that has studied, for example, the extrapolation of load spectrum in the whole lifespan cycle [9] and the minimum sample size of load collection under typical working conditions [10], along with a multi-dimensional damage study of a comprehensive load spectrum [11]. In addition to the in-depth study of load spectrum, it is important to ensure the accuracy of modeling objects as much as possible. The wheel-side electric drive system has a short transmission chain, which eliminates the need for traditional parts such as a differential, half shafts, and a universal joint. Therefore, the gears of a wheel-side electric drive system are critical to output robustness and NVH performance. The study of gear strength has a long history. The Lewis formula for calculating bending strength proposed by Lewis in 1890 and the Hertz formula for calculating contact strength proposed by Hertz in 1891 have laid the theoretical foundation for calculating gear bending and contact strength, respectively [12]. On this basis, with the continuous deepening of theoretical research, various methods for calculating the bearing capacity of gears have been proposed. Some countries have established industry standards for gear strength, such as the ISO (International Organization for Standardization) TC 60/SC 2/WG 6 formulas [13]; the DIN (Deutsche Industry Norm) standard 3979-1979 [14]; the AGMA (American Gear Manufacturers Association) standard formulas [15]; the JMS (Japanese Mechanical Society) formulas [16], etc. With the rapid development of computer technology in contemporary times, various commercial gear analysis software programs have emerged [17], such as Masta, Romax, Kisssoft, etc. Due to the high correlation between the tooth root fillet curve and the machining process, commercial software cannot predict and exhaustively list the actual machining status, so it is usually replaced by an approximate equivalent method [18]. However, for gears with high precision and harsh working loads, the fillet is a sensitive factor in FEM (finite element method) analysis, especially in the bending strength of the tooth root [19]. For the wheel-side electric drive system, its gears are processed by hobbing and form grinding, which can modify the gear tooth profile in a free-style way [20]. Form grinding uses a specially refined grinding wheel to meet the customized requirements so that a high quality of tooth precision and surface quality is guaranteed [21,22]. Therefore, it is necessary to conduct precise tooth profile modeling for the process of hobbing and form grinding, which is decisive for the correctness of simulations and tests.

In Section 2, the research object is introduced, including the structure of the wheel-side electric drive system and the modeling of the transmission system. In Section 3, the research method is discussed in detail, including the tooth profile precise calculation, the design parameters of gears, and the load spectrum analysis and equivalent transformation theory for various model working conditions. In Section 4, the prototype development and bench test validation are discussed and presented. Finally, several conclusions are summarized in Section 5.

2. Research Object

The wheel-side electric drive system is a flexible module that is installed on the rear suspension, as shown in Figure 1. Compared with the traditional centralized electric drive system, the wheel-side electric drive system eliminates the differential, the universal joint, the drive half shaft, and other components. Instead, it integrates the functions of the powertrain assembly, suspension assembly, and transmission axle assembly together. As a result, the wheel-side electric drive system has the advantages of compact structure and high transmission efficiency [6]. A three-phase permanent magnet synchronous motor (PMSM) works as the drive power, with the technical parameters shown in Table 1.

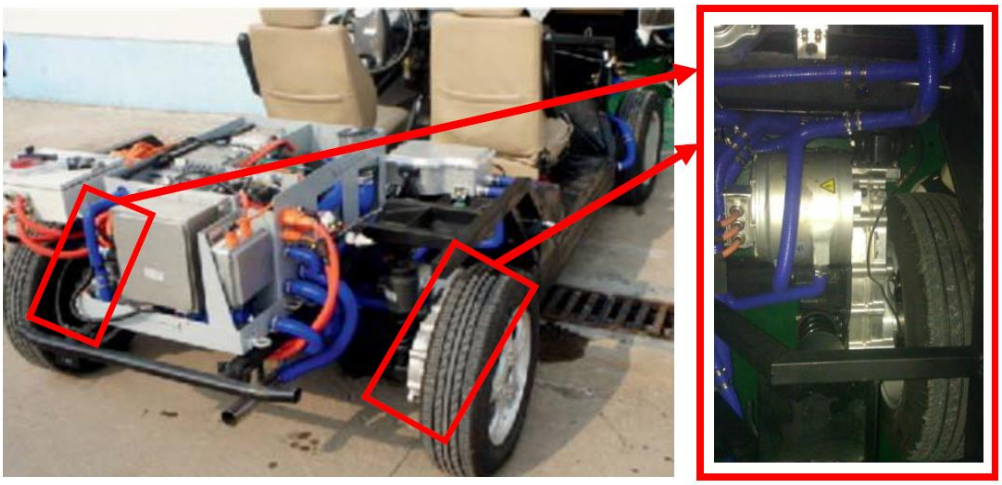


Figure 1. Vehicle prototype with the wheel-side electric drive system.

Table 1. Parameters of the PMSM.

Technical Parameters	Data Index
Rated power (kW)	15
Peak power (kW)	25
Rated speed (r/min)	4000
Rated torque (Nm)	35.8
Peak torque (Nm)	90
Speed range (r/min)	0~9500

According to the patent [4], the basic structure of the wheel-side electric drive system is shown in Figure 2. In this system, the PMSM drives the input shaft and 1# stage driving gear. The power goes through the 1# stage driving gear, the 1# stage driven gear, the inter-mediate shaft, the 2# stage driving gear, the 2# stage driven gear, and the output shaft. The output shaft is assembled with a wheel sleeve and a hub bearing, ultimately connected to the wheel. All the shafts mentioned above are mounted on the housing. The housing is connected to the main frame through a rubber hinge, and the spring and damper are also fixedly installed on the corresponding position. By defining the relative positional

relationship of the housing, spring, and damper, the housing acts as a suspension arm with the hinge.

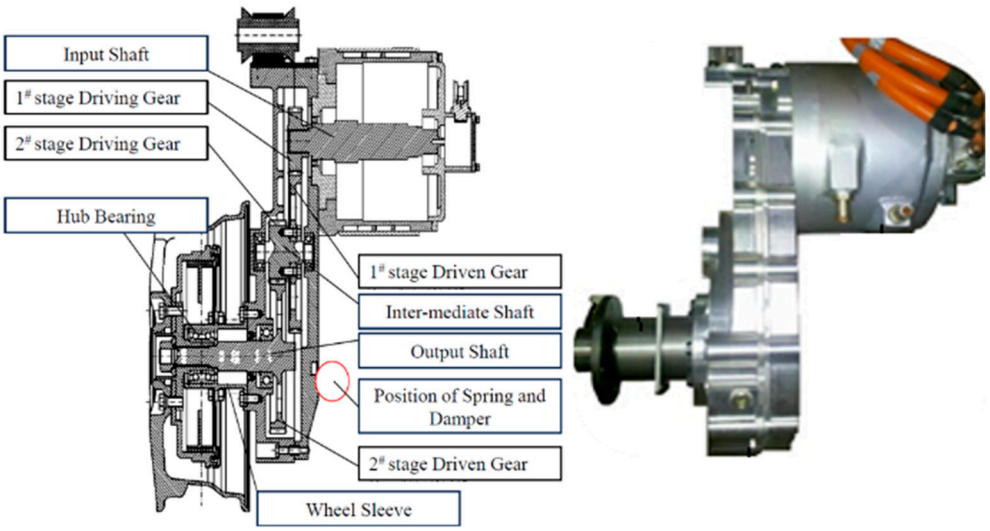


Figure 2. Structure of the wheel-side electric drive system.

The wheel-side electric drive system is driven by two-stage fixed axis helical gears. Among them, the 1# stage driving gear is directly fixedly connected to the motor rotor shaft, so there are no bearings in the gearbox, but the positioning is directly achieved by the bearings on the motor rotor shaft. The 2# shaft is supported by two deep groove ball bearings, while the axial force can be significantly counteracted by the reasonable design of a gear helix angle. Due to the presence of hub bearings, the 3# stage shaft has a strong load-bearing capacity, with a deep groove ball bearing-assisted positioning. The model is shown in Figure 3.

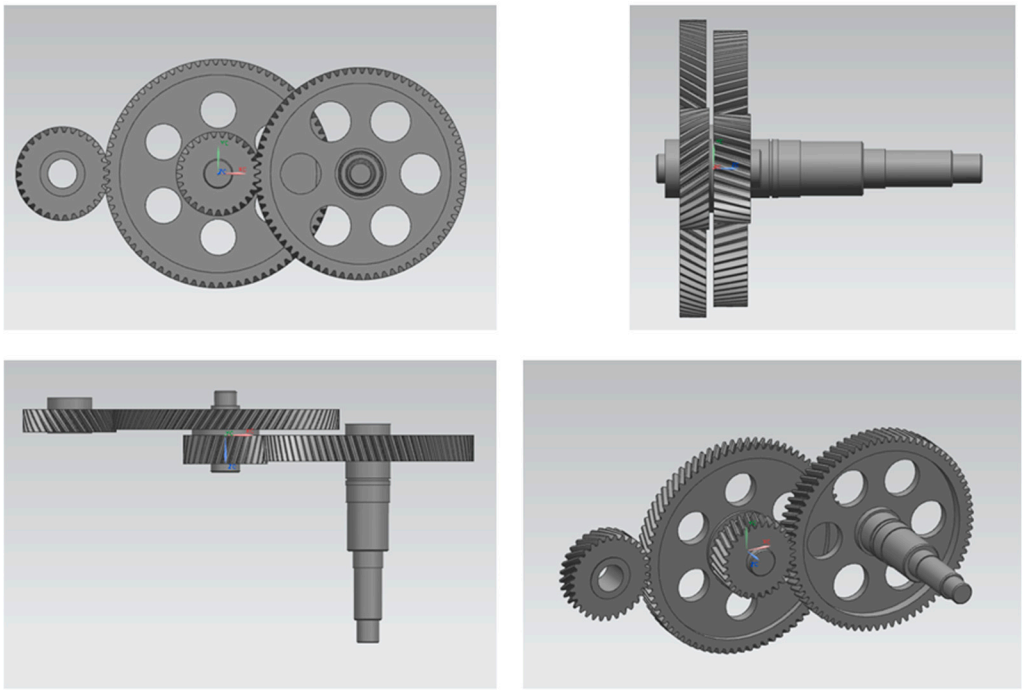


Figure 3. Modeling of the transmission system.

For the gear parts of the transmission system, they follow the processing flowchart, as Figure 4 shows. After the basic processing of forging, normalization, and turning, the gears

are ready for hobbing and chamfer. After that, the gears are sent to the heat treatment with carburizing quenching. Then, the thermal deformation must be checked to see whether the parts are ready for form grinding. If they are not ready, then the process parameters in hobbing must be adjusted to improve the thermal deformation. If they are ready, the parts are sent to undergo the process of form grinding.

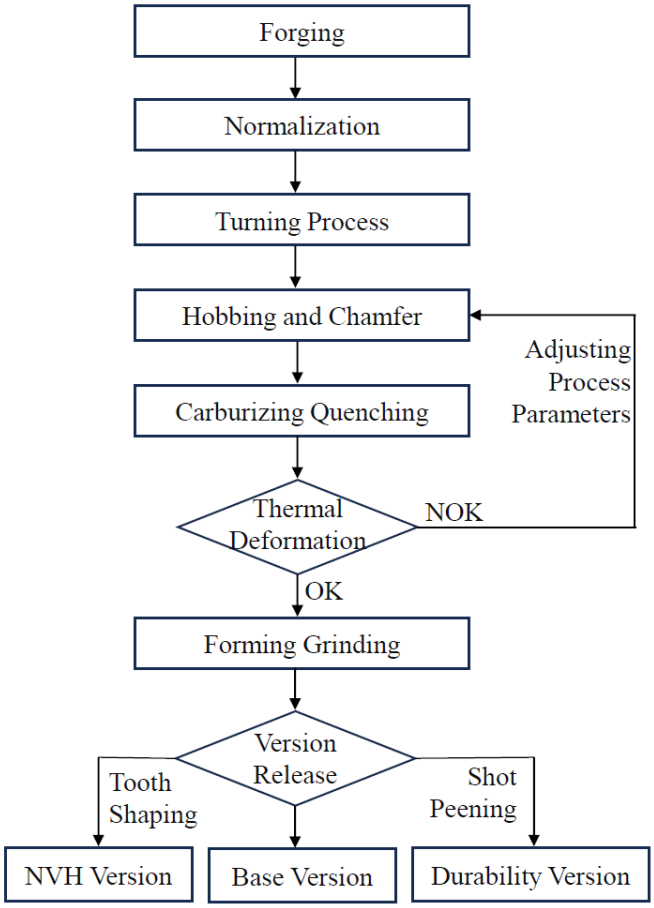


Figure 4. Processing flowchart of the gears.

The chassis with awheel-side electric drive system presents a highly modularized design, which can adapt to different types of vehicles, such as city sedans, off-road vehicles, sightseeing vehicles, or golf carts. Correspondingly, the gear tooth profile can be specially modified and tuned according to the specific operating conditions of the vehicle. In gear processing, the free shaping function of form grinding can realize these customization requirements. The final release version can be divided into three categories. The base version is the original state of form grinding, which can cover the basic demand of the vehicle. If the wheel-side electric drive system is supposed to be equipped with vehicles of high NVH demand, such as tourist sightseeing cars or golf carts, then a special tooth shaping can be conducted by the refinement of form grinding a wheel case by case. On the other hand, if the wheel-side electric drive system is supposed to be equipped with vehicles of high durability demand such as taxis, then a shot peening process can be conducted to improve the tooth contact fatigue strength. According to the different coverage rates of shot peening, the contact strength of the tooth surface can be increased by 10% to 20% [23]. But this is at the cost of NVH performance, as shot peening will affect the condition of the tooth surface. Figure 5 shows the modular system adapted to different vehicle models.

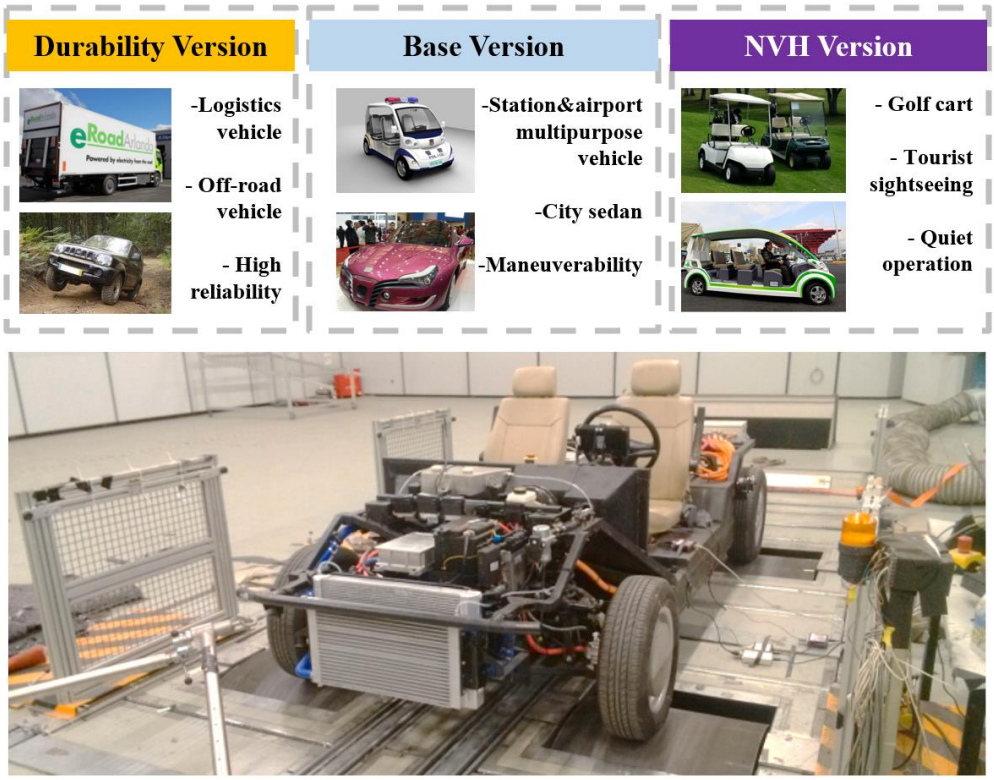


Figure 5. Modular chassis adapted to different vehicle models.

3. Research Method

3.1. Tooth Profile Precise Functions Solving

According to the discussion above, the most significant process that determines the gear precision is hobbing and grinding. The tooth curve of the gear is shown in Figure 6, in which the involute part and root fillet curve are generated by hobbing. Then, a chamfer is manufactured to the gear, with a grinding allowance for the final grinding. Grinding teeth prohibits machining tooth root circles, as residual stress is crucial for tooth root bending strength [24]. When the feed parameters for grinding teeth are not set properly, there is a possibility of step formation in the tooth root circle and fillet curve. This will lead to the risk of tooth breakage, which is unacceptable. As a result, grinding allowance is the most important factor in the process coordination between hobbing and grinding. If the grinding allowance is too narrow, then the SAP (Start of Active Profile) points will be affected. If the grinding allowance is too large, then the effective hardening layer depth generated by heat treatment will be polished, which will have a negative effect in the contact fatigue life of the tooth surface [25]. According to experience data, the ideal value of grinding allowance is around 0.1 mm, which may have slight fluctuations within the specific gear parameters. The surface roughness of the tooth can be Rz16 after hobbing and is able to reach Rz4 after form grinding.

The root fillet curve is generated by hobbing, which is directly related to the bending strength of the tooth root. According to the literature [26], the normal plane coordinate system of the hob is shown in Figure 6. Among them, LM is the straight part of the hob blade, MN is the corner part of the hob blade, Q is the center of the hob corner, r is the corner radius of the blade, α_n is the pressure angle, m is the modulus of the hob, δ is the center of the corner of the blade to the center line of the hob, and E is the distance from the starting point M of the knife edge fillet to the center line. In Figure 7, all the distance relationships between the center line and each geometric element are marked.

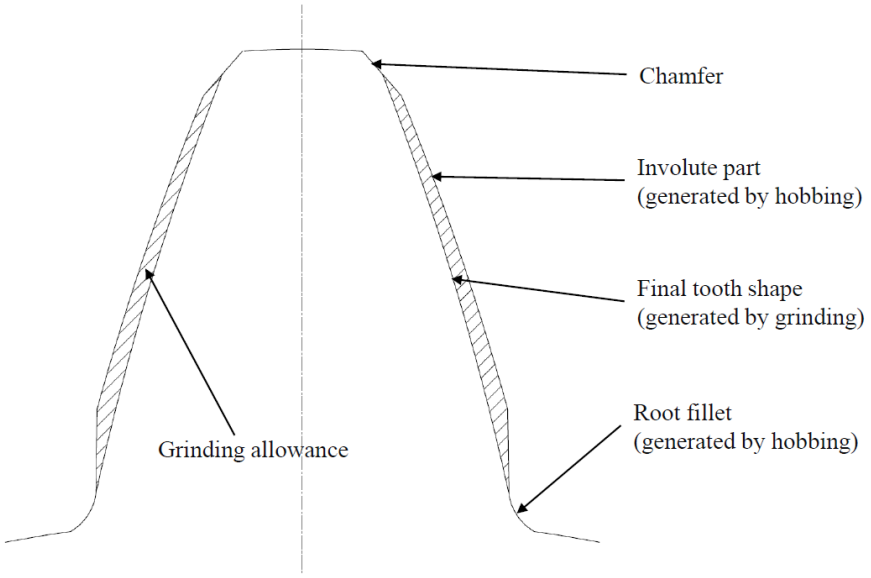


Figure 6. Tooth curve of gear with process of hobbing and form grinding.

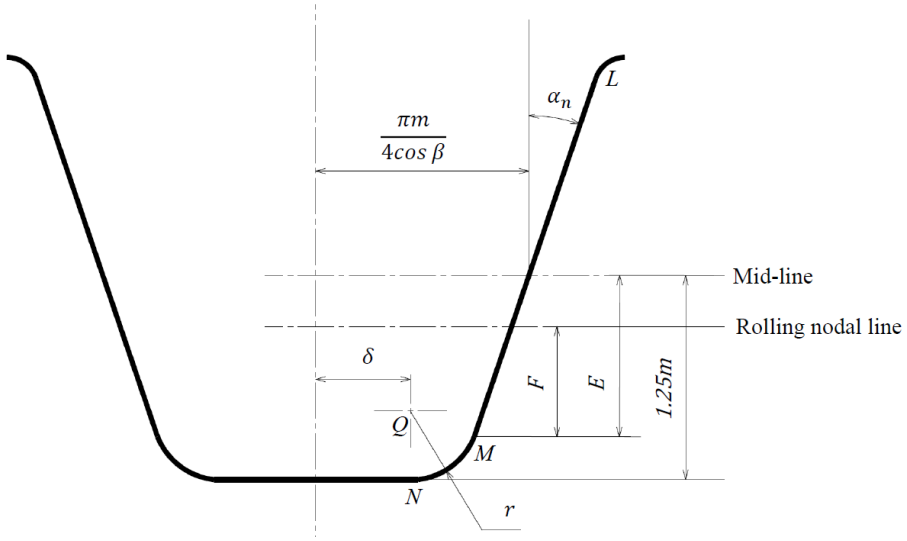


Figure 7. The normal plane coordinate system of the hob.

The expression of the linear blade LM and relevant relationship can be described as in Equations (1)–(4):

$$x_1 = (y_1 - xm)\tan\alpha_n - \frac{\pi m}{4\cos\beta} \quad (1)$$

$$E = 1.25m - r + r\sin\alpha_n \quad (2)$$

$$F = 1.25m - xm - r \quad (3)$$

$$\delta = \frac{\pi m}{4} - E\tan\alpha_n - r\cos\alpha_n \quad (4)$$

where m is the hob modulus, α_n is the pressure angle, x is the displacement coefficient, and β is the helix angle.

The gear tooth of the helical gear and the axis are inclined into a spiral shape, and the intersection angle formed is the helix angle β. In accordance with the literature [27], the geometric relationship of the hob machining gear is shown in Figure 8. O_2 is the center of the gear blank to be processed and P is the meshing node of the hob cutter and the gear blank. We can make X-P-Y a fixed coordinate system with X_1-O_1-Y_1 as the coordinate system fixed on the hob; we can also move the rolling pitch line to be on the O_1X_1 axis,

which coincides with the fixed coordinate axis PX and move the hob to be on the O_1Y_1. The distance between the hob coordinate axis O_1Y_1 and the fixed coordinate PY axis is S, which is the meshing line of the pressure angle α_n passing through the point P. ψ is the angle between PK and PX, and $\varnothing$ is the angle between O_2Y_2 and O_2Y. In the process of gear hobbing, the hob moves to the left to perform cutting action. The X_1-O_1-Y_1 coordinates also move to the left with the hob, and pure rolling is maintained between the gear pitch circle and the hob hobbing straight line.

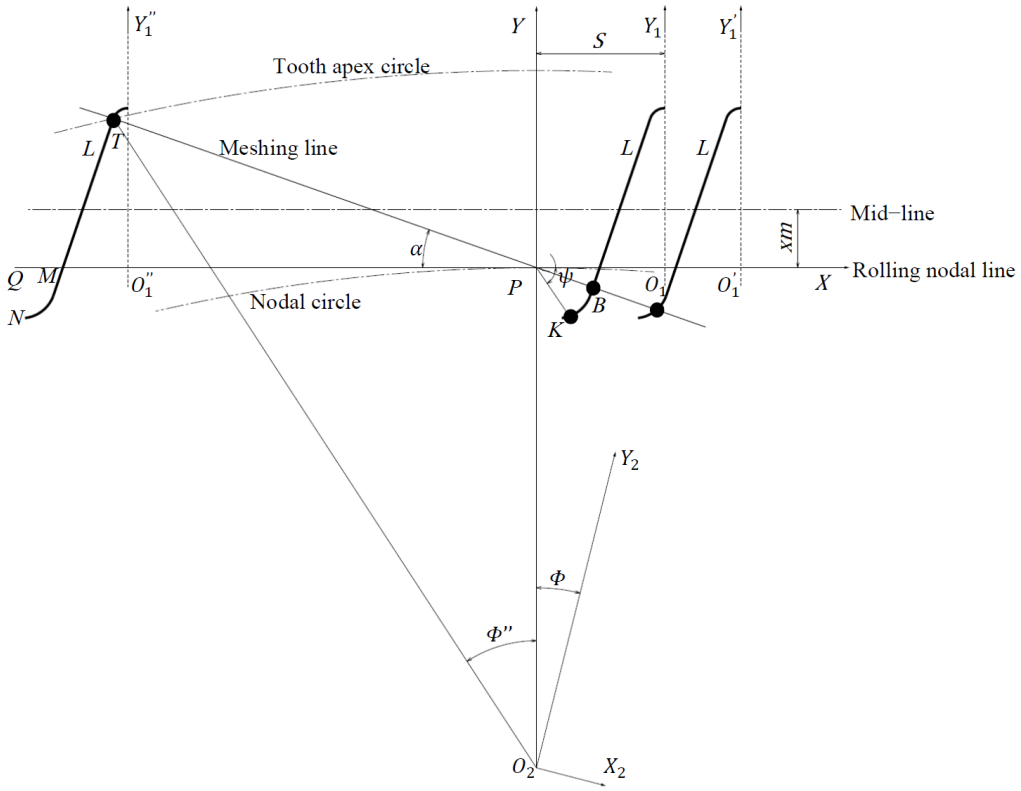


Figure 8. Geometric relationship of the hobbing process.

The tooth profile can be divided into the involute part and the root fillet curve. Among them, the involute part is formed by the straight part LM of the blade. Point M is the lowest point of the straight part of the blade, and point T is the intersection point between the meshing line and the straight blade. When the X_1-O_1-Y_1 coordinate system is at the position of X'_1-O'_1-Y'_1, the meshing line is just past the M point, and the lowest point of the tooth-shaped involute part is cut out at this time. As the hob moves to the left, the cutting point also moves upwards. When the X_1-O_1-Y_1 coordinate system is at the position of X''_1-O''_1-Y''_1, the T point is exactly on the addendum circle, and the involute part of the tooth profile is completed at this time. While cutting the involute part, the blade fillet MN forms a fillet curve, and its instantaneous cutting point is the intersection of the extension line of PQ and the arc MN. When the X_1-O_1-Y_1 coordinate system is at the position of X'_1-O'_1-Y'_1, the extension line of PQ intersects the arc MN at point M, and the tooth fillet curve starts. As the rack moves to the left, the angle ψ between PQ and PX gradually increases; when $\psi = 90°$, the PQ and PY axes coincide to complete the cutting of the involute part.

The analytical formula of the meshing line TM is

$$x_1 + y_1 \cot \alpha_n = -S \tag{5}$$

The tooth profile of a helical gear is a set of spatial curves which are parallel to the end face with the helix angle of β. Combine the vertical formulas above to obtain the coordinates of point B (x_B,y_B):

$$\begin{cases} x_B = -S - \frac{\cos\alpha_n}{\tan\alpha_n + \cot\alpha_n}\left(\frac{\pi m}{4\cos\beta} - S + xm\tan\alpha_n\right) \\ y_B = \frac{\left(\frac{\pi m}{4\cos\beta} - S + xm\tan\alpha_n\right)}{(\tan\alpha_n + \cot\alpha_n)} \end{cases} \tag{6}$$

As the tool gradually moves to the left, the S value continuously changes, which corresponds to a series of continuously changing B point coordinates.

The radius of the hob blade edge becomes an ellipse on the conjugate plane, the radius of the minor axis is still r, and the radius of the major axis becomes $r/\cos\beta$. From this, the expression of the blade ellipse can be obtained as Equations (7) and (8):

$$\frac{\left(x_1 + \frac{\pi m}{2\cos\beta} - \frac{\delta}{\cos\beta}\right)^2}{\left(\frac{r}{\cos\beta}\right)^2} + \frac{(y_1 + 1.25m - r)^2}{r^2} = 1 \tag{7}$$

$$l = \frac{r\cos\alpha_n}{\cos\beta} \tag{8}$$

Then, the coordinates of M point can be obtained as (x_M, y_M):

$$\begin{cases} x_M = \frac{-\left(\frac{\pi m}{2} - \delta - r\cos\alpha_n\right)}{\cos\beta} \\ y_M = -[1.25m - r(1 - \sin\alpha_n)] \end{cases} \tag{9}$$

According to the literature [28], the normal of the cutting point at every moment in the cutting process must pass through the meshing node, thereby determining the position of the K point. Suppose the coordinates of point K are (X_K, Y_K), then the equation of the line PK is as follows:

$$\xi + \frac{\eta}{\tan\psi} = -S \tag{10}$$

The point (ξ, η) is the center of curvature corresponding to the point (x,y) on the curve y = f(x), and its advanced mathematical definition is described in Equations (11) and (12):

$$\xi = x - y'\frac{1 + y'^2}{y''} \tag{11}$$

$$\eta = y + \frac{1 + y'^2}{y''} \tag{12}$$

The corresponding K point coordinates meet the following:

$$\xi + \eta Y'_K = X_K + Y_K Y'_K \tag{13}$$

With the following additional formula:

$$\tan\psi = \frac{1}{Y'_K} \tag{14}$$

Combining the Equations (11)–(14) above, we can obtain

$$\xi + \eta Y'_K = -S \tag{15}$$

With a series value of S, the K point coordinates can be obtained.

So far, the solution of the conjugate surface of the hob has been completed. Next, the corresponding positions of the cutting points B and K are determined on the processed gear blank. In order to facilitate further programming calculations, the method described in the literature (Zhang, 2011) [27] needs to be used for coordinate transformation. Suppose the coordinate system on the gear to be processed is $X_2O_2Y_2$; make the transitional relationship of R (the gear pitch circle radius) as Equation (16):

$$S = R\psi \tag{16}$$

Then, the coordinate system X_1-O_1-Y_1 and the coordinate system X_2-O_2-Y_2 relationship will be as follows:

$$\begin{cases} x_2 = (S + x_1)\cos\varphi - (R + y_1)\sin\varphi \\ y_2 = (S + x_1)\sin\varphi - (R + y_1)\cos\varphi \end{cases} \tag{17}$$

According to the formulas above, the coordinate transformation between the coordinate system X_1-O_1-Y_1 and the coordinate system X_2-O_2-Y_2 can be realized, and the calculation of the end face tooth profile of the helical gear is completed.

Finally, the tooth profile of each section parallel to the section needs to be solved. The offset angle θ of the front and rear ends of the helical gear on the X-O-Y plane is described as follows:

$$\theta = \frac{b}{R\cot\beta} \tag{18}$$

In Equation (18), b is the tooth width, R is the index circle radius, and β is the helix angle. This is in addition to the following Their geometric relationship comes as following:

$$R = \frac{mz}{2\cos\beta} \tag{19}$$

Combining the Equations (18) and (19) above, we can obtain:

$$\theta = \frac{2b\sin\beta}{mz} \tag{20}$$

Suppose the coordinates of a point G on the tooth profile of the front face are (x_G, y_G), and the coordinates of point G′ G′ on the corresponding back face are $(x_{G'}, y_{G'})$, then we can ultimately obtain Equation (21):

$$\begin{cases} x_{G'} = y_G\sin\theta + x_G\cos\theta \\ y_{G'} = y_G\cos\theta - x_G\sin\theta \end{cases} \tag{21}$$

For different sections, the value of θ changes according to the value of b, and the corresponding tooth profile of all sections are obtained consecutively.

3.2. Gear Parameters

The wheel-side electric drive system is a fusion of a vehicle powertrain and suspension system. Because the housing is supposed to act as the suspension trailing arm, the 1# stage driven gear and the 2# stage driven gear are expected to be similar in size. According to the dimension requirement of the of the trailing arm length, the center distance between the 1# stage shaft and 3# stage is defined as 270 mm. And the vehicle power calculation supports the total transmission ratio of a two-stage gear so that it can reach 6.6. The parameters of the gears are shown in Table 2.

Table 2. Parameters of the gear train.

	1# Stage Driving Gear	1# Stage Driven Gear	2# Stage Driving Gear	2# Stage Driven Gear
Tooth Number	$z_{11} = 31$	$z_{12} = 78$	$z_{21} = 29$	$z_{22} = 76$
Tooth Modulus (mm)	$m_{n1} = 2.1$	$m_{n1} = 2.1$	$m_{n2} = 2.3$	$m_{n2} = 2.3$
Helix Angle (°)	$\beta_{n1} = 34$	$\beta_{n1} = 34$	$\beta_{n2} = 22$	$\beta_{n2} = 22$
Displacement Coefficient	$x_{n11} = 0.3$	$x_{n12} = 0.1$	$x_{n21} = 0.31$	$x_{n22} = -0.03$
Pressure Angle (°)	$\alpha = 20$	$\alpha = 20$	$\alpha = 20$	$\alpha = 20$
Addendum Height Coefficient	$h_{a1n} = 1.3$	$h_{a1n} = 1.3$	$h_{a2n} = 1.24$	$h_{a2n} = 1.24$
Width (mm)	$b_{11} = 20$	$b_{12} = 18$	$b_{21} = 25$	$b_{22} = 23$
Base Circle Diameter (mm)	$d_{b11} = 71.901$	$d_{b12} = 180.911$	$d_{b21} = 66.964$	$d_{b22} = 175.491$
Pitch Circle Diameter	$d_{p11} = 78.995$	$d_{p12} = 198.763$	$d_{p21} = 72.289$	$d_{p22} = 189.446$
Center Distance (mm)	$a_1 = 139$	$a_1 = 139$	$a_2 = 131$	$a_2 = 131$
End-face Coincidence	$\varepsilon_{\alpha 1} = 1.629$	$\varepsilon_{\alpha 1} = 1.629$	$\varepsilon_{\alpha 2} = 1.812$	$\varepsilon_{\alpha 2} = 1.812$
Axial Coincidence	$\varepsilon_{\beta 1} = 1.526$	$\varepsilon_{\beta 1} = 1.526$	$\varepsilon_{\beta 2} = 1.192$	$\varepsilon_{\beta 2} = 1.192$
Total Coincidence	$\varepsilon_{r1} = 3.155$	$\varepsilon_{r1} = 3.155$	$\varepsilon_{r2} = 3.004$	$\varepsilon_{r2} = 3.004$
Reduction Ratio	$i_1 = 2.516$	$i_1 = 2.516$	$i_2 = 2.621$	$i_2 = 2.621$

3.3. Load Spectrum Analysis and the Equivalent Transformation

When the vehicle is driving, the wheel-side electric drive system is subjected to the alternating loads. For high cycle loads (with a failure life longer than 10^3 cycles), the nominal stress method is usually used in conjunction with the S-N curve to evaluate the durability of the system. According to the speed variation of the vehicle under typical operating cycle conditions [29], the PMSM follows the vehicle speed to obtain the corresponding motor output characteristic curve, including the timing records of output torque and output speed, as shown in Figure 9.

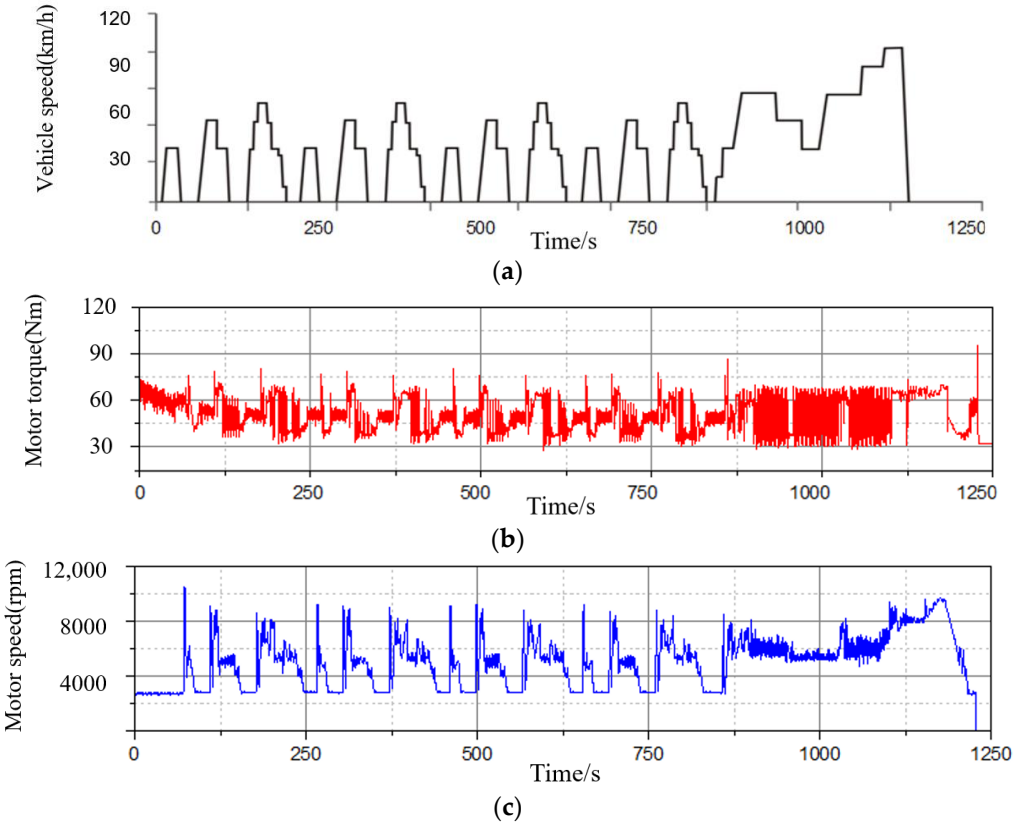
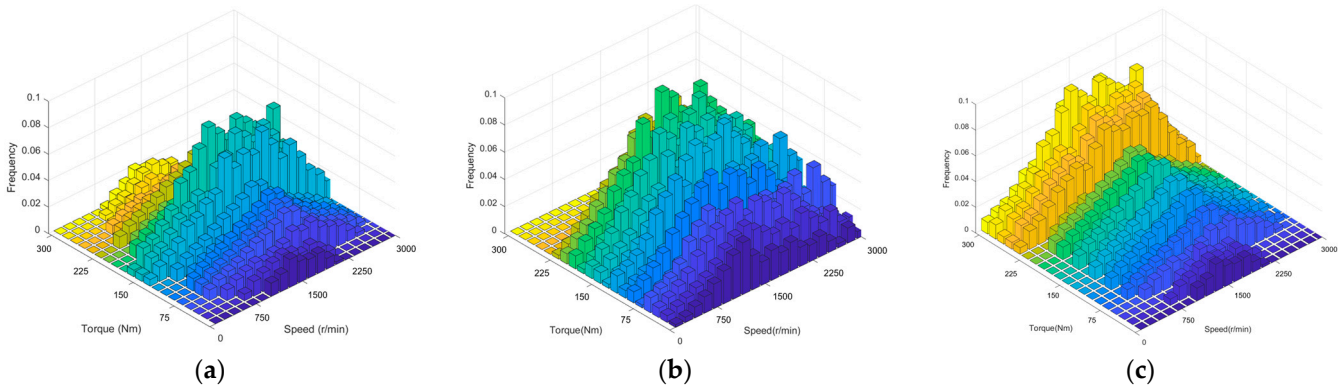


Figure 9. Typical operating cycle conditions of vehicle. (**a**) Vehicle speed curve in time domain. (**b**) Motor torque curve in time domain. (**c**) Motor speed curve in time domain.

Based on the typical operating cycle conditions, we use the rain flow methodology to count the working conditions of the basic version, NVH version, and durability version, respectively. The histograms of working condition frequency are presented in Figure 10.



(**a**) (**b**) (**c**)

Figure 10. Histogram of load spectrum of each version working condition. (**a**) Basic version. (**b**) NVH version. (**c**) Durability version.

When studying the limit value of load extrapolation, it is generally considered that 10^3 cycles of the over value cumulative cycle is a sufficiently representative order of magnitude [30]. The mathematical expression is as follows:

$$1 - F(T_{max}) = 10^{-6} \tag{22}$$

where $F(T)$ is the cumulative distribution function and T_{max} is the maximum torque of load sample statistics. Based on this, the fatigue strength index can be expressed as follows:

$$b = \frac{lgS_{1000} - lgS_{be}}{lg10^3 - lg10^6} = -\frac{S_{1000}}{3S_{be}} \tag{23}$$

where b is the fatigue strength index and S_{1000} is the fatigue strength at 1000 cycles. S_{be} is the fatigue strength of the sample.

The criterion for developing the extrapolated load spectrum is to omit the small load cycles that fall below the material fatigue limit [31]. We set the filtering threshold to be 55% of the fatigue limit of the smooth specimen. The corresponding stress amplitude is 98.2 Mpa, with the load below this amplitude being omitted. According to the Miner principle of linear cumulative damage [32], the comprehensive load spectrum of the gears is formulated, as shown in Figure 11. There are nine stages of equivalent load in total, which can cover the working conditions of the basic version, the NVH version and the durability version. The maximum stress amplitude is 556 MPa, with a corresponding motor torque of 90 Nm, and a S-N curve value of 9330 times. The S-N curves of the material and sample are both shown in Figure 12.

Considering the impact coefficient, the maximal motor torque is multiplied by 1.5 times as the input load. The FEM result is shown in Figure 13. The maximum contact stress of the 1# stage driving gear is 419.72 MPa on the gear root. The maximum stress of the 1# stage driven gear is 452.21 MPa on the gear root. The maximum stress of both the 2# stage driving gear and the 2# stage driven gear is 864.91 MPa, which appears in the tooth surface contact position.

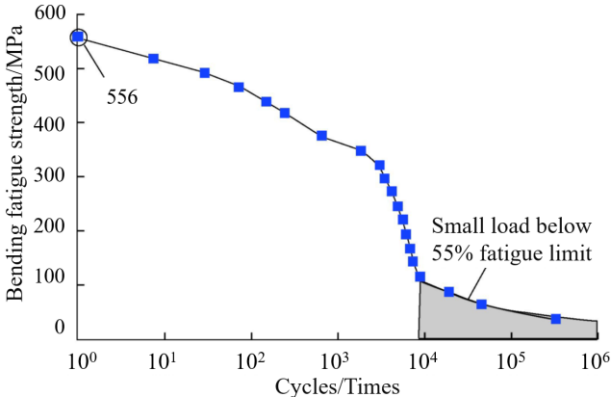


Figure 11. Gear stresses with the comprehensive load spectrum.

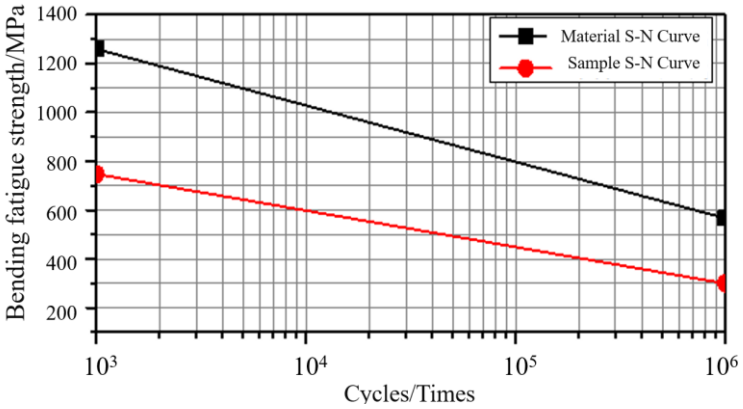


Figure 12. S-N curve of 20CrMnTi.

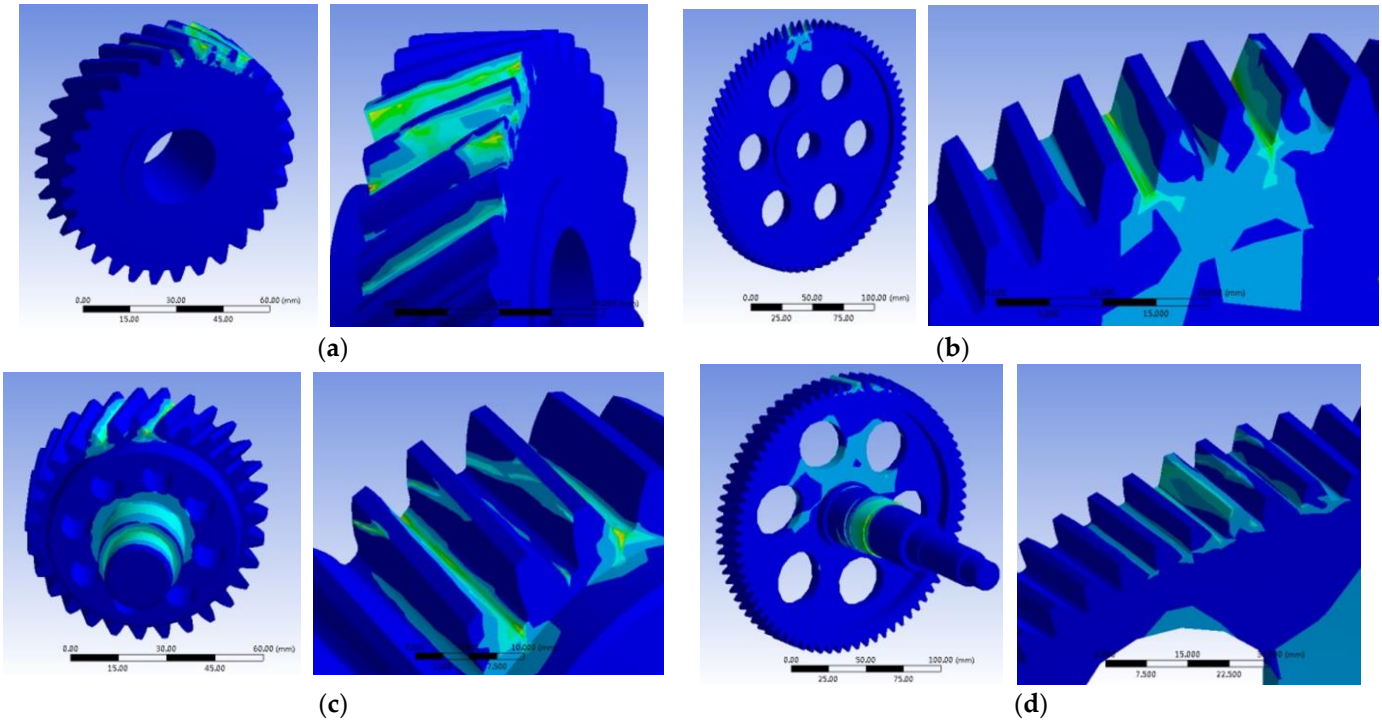


Figure 13. FEM stress analysis results. (**a**) Stress nephogram of the 1# stage driving gear. (**b**) Stress nephogram of the 1# stage driven gear. (**c**) Stress nephogram of the 2# stage driving gear. (**d**) Stress nephogram of the 2# stage driven gear.

Considering the severity of a tooth root fracture, we pay special consideration to the tooth root strength. Based on the FEM analysis data, the fatigue damage states of each gear are presented in Table 3. We can see that the 2# stage driving gear is the most vulnerable component of the system.

Table 3. Fatigue damage status of the gear train.

	Tooth Root Bending Stress	Fatigue Life Under S-N Curve	Equivalent Damage Rate of Every Single Load
1# stage Driving Gear	200.99 MPa	16,477,915	0.000107182
1# stage Driven Gear	186.55 MPa	87,526,966	0.002301166
2# stage Driving Gear	384.44 MPa	250,309	0.001189999
2# stage Driven Gear	364.47 MPa	283,375	0.000000086

4. Development and Validation

4.1. Prototype Development

After theoretical analysis and FEM simulation, a prototype is made and taken to the test bench to conduct the relevant experiment for validation. We take the 1# stage driving gear as an example. Figure 14 shows the tooling and sample, with the corresponding gear hob and a grinding wheel. From the appearance of the sample, the root fillet curve, the involute part, and the chamfer are clearly presented, which meets the expectation of design and process.

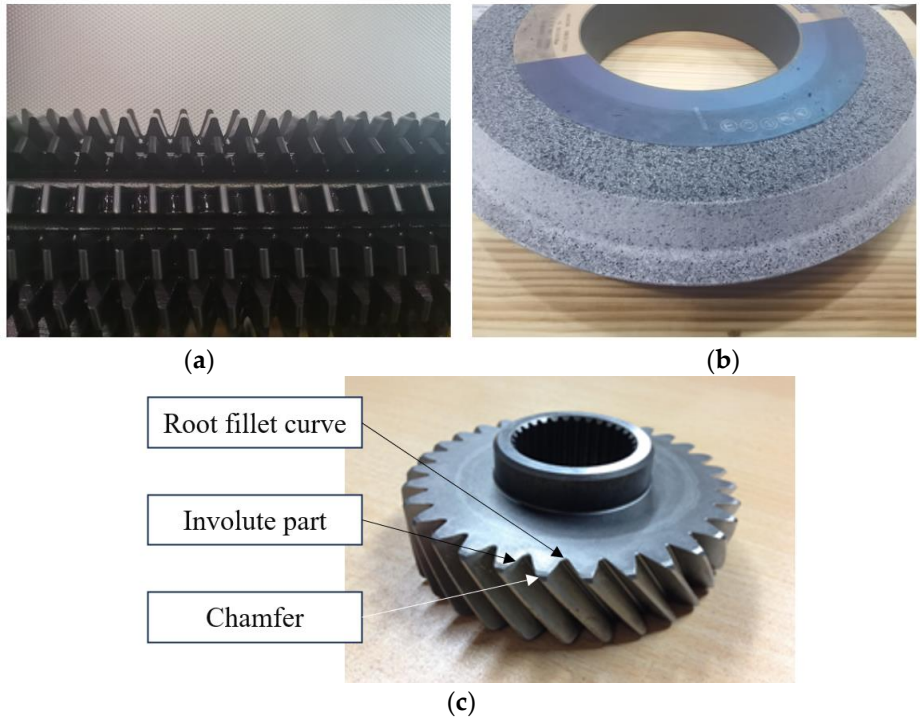


Figure 14. Tooling and sample of the gear. (**a**) Gear hob. (**b**) Grinding wheel. (**c**) Sample of the 1# stage driving gear.

With the process of hobbing and form grinding, the accumulated errors of each gear are shown in Figure 15. The difference in modulus in the 1# and 2# stage gears leads to a slight change in Fr (concentricity deviation) and Fp (total pitch deviation). Usually, the cumulative error increases slightly with the increase in gear teeth number and tip circle diameter. The results show that all the gears are all at the accuracy level of 6. The gear

adopts 20CrMnTi material, with the surface being carburized, quenched, and tempered. The surface hardness is HRC 62~65, while the core hardness is HRC 30~45, and the contact fatigue limit corresponds to 1500 MPa.

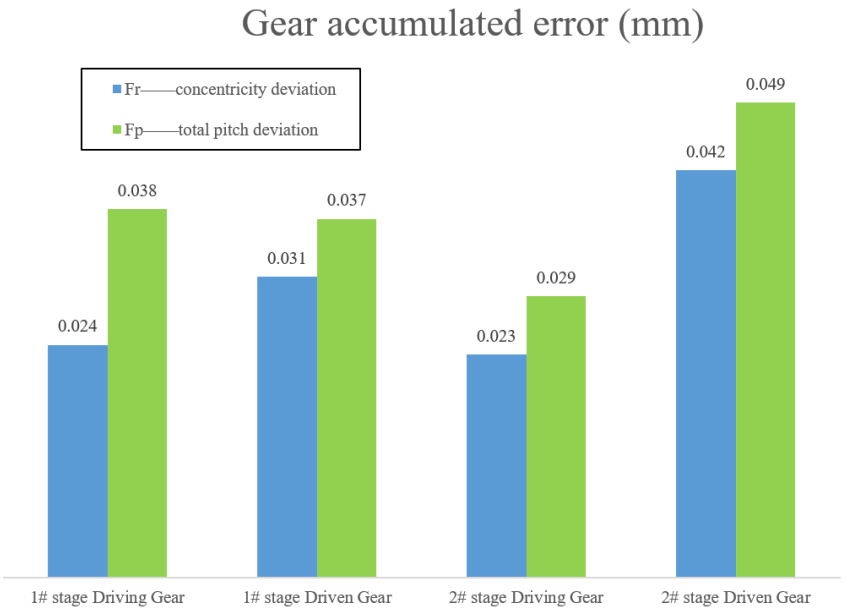


Figure 15. Grinding accuracy of the gear samples.

4.2. Bench Test

A test bench is built for the wheel-side electric drive system, which simulates the changes in wheel speed, torque, and vertical load during the movement of the whole vehicle. In this way, a durability test of the wheel-side electric drive system is conducted. The wheel-side electric drive system equipped on the durability bench is shown in Figure 16.

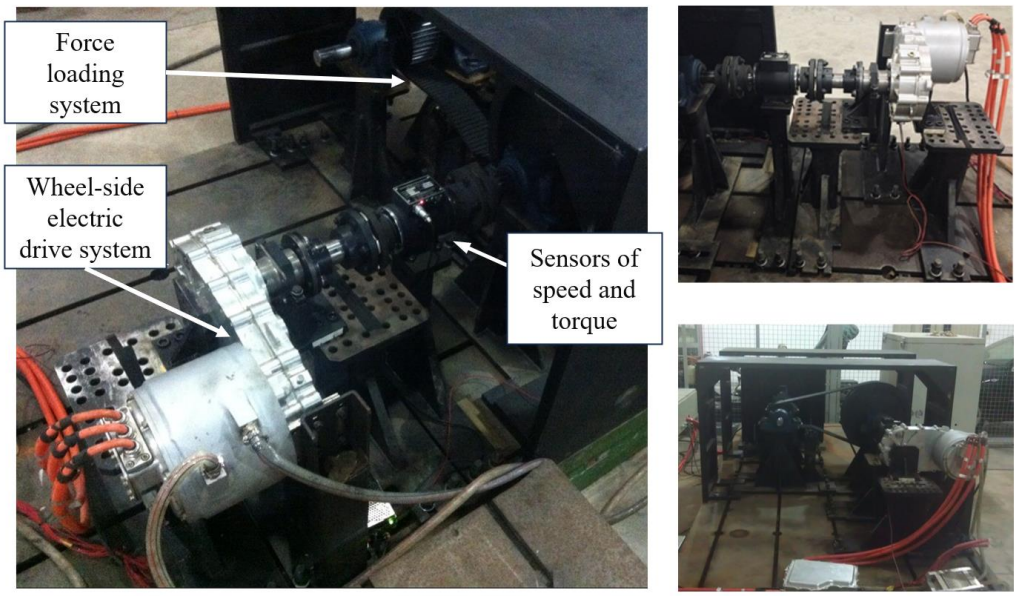


Figure 16. The durability test bench.

The purpose of the reliability test is to verify the ability of the wheel-side electric drive system to work normally under the specified conditions and within the specified time [33]. Therefore, the judging standard of the reliability test is whether the prototype can work normally before the end of the test. The wheel-side electric drive system needs to

undergo a warm-up cycle initially, which is significant to ensure that all the components are fully engaged and matched, eliminating the unevenness and inconsistency that may occur during assembly. The durability cycle consists of three parts, namely the warm-up cycle, the driving cycle, and the regenerative braking cycle. The driving cycle consists of nine stages, while the regenerative brake cycle has the corresponding nine stages with the same speed and the opposite torque. Once the test starts, it is supposed to continue for at least one cycle without stopping. If there is an emergency where the test bench needs to be checked. The loading procedure of the durability test is shown in Table 4.

Table 4. Operation procedures of a single cycle in the comprehensive test.

		Motor Torque	Motor Speed	Test Time (per Cycle)
Warm-Up Cycle		**36 Nm**	1800 r/min	30 min
Driving cycle	1# stage	90 Nm	4000 r/min	5 min
	2# stage	77 Nm	4000 r/min	18 min
	3# stage	68 Nm	4000 r/min	22 min
	4# stage	60 Nm	4000 r/min	25 min
	5# stage	51 Nm	4000 r/min	18 min
	6# stage	43 Nm	4000 r/min	16 min
	7# stage	35 Nm	4000 r/min	15 min
	8# stage	26 Nm	6000 r/min	8 min
	9# stage	18 Nm	9000 r/min	3 min
Regenerative braking cycle	1# stage	−90 Nm	4000 r/min	5 min
	2# stage	−77 Nm	4000 r/min	18 min
	3# stage	−68 Nm	4000 r/min	22 min
	4# stage	−60 Nm	4000 r/min	25 min
	5# stage	−51 Nm	4000 r/min	18 min
	6# stage	−43 Nm	4000 r/min	16 min
	7# stage	−35 Nm	4000 r/min	15 min
	8# stage	−26 Nm	6000 r/min	8 min
	9# stage	−18 Nm	9000 r/min	3 min

In Table 4, the damage of the shown single cycle test can cause an equivalent damage of 0.527% of the whole fatigue limit. The Table 4 collects the information of a single cycle test, which can cause an equivalent damage of 0.527% of the whole fatigue limit. According to the Miner principle of linear cumulative damage, the whole test is made up of 120 cycles in total, which is an equivalent conversion of durability mileage of 150,000 km. In the comprehensive test, the cumulative damage of the system is estimated to be 63.27%. According to the theoretical conversion, the equivalent damage in the base version is 52.15%, while the durability version is 60.61%, and the NVH version is 45.29%. It is proved that the comprehensive test loading conditions can cover all three of the expected versions. The detailed information of the test bench and the 2# stage driving gear (the most vulnerable component of the system) is presented in Table 5.

During the test period, the test bench runs normally without stopping. The warm-up cycle only runs once at the very beginning and then the driving cycle and the regenerative braking cycle alternatively continues. The monitored temperature of the housing reaches its highest temperature of 59 °C, which proves the stable running status of the system. The monitored noise is below 70 dB without rattling or whining, which meets the NVH performance goal.

Table 5. Fatigue information of theoretical calculation.

Test Item	Test Data
Equivalent damage of a single cycle	0.527%
Cumulative damage of the total durability test (150,000 km)	63.27%
Equivalent damage in the base version	52. 15%
Equivalent damage in the durability version	60.61%
Equivalent damage in the NVH version	45.29%
Loading time of a single cycle (min)	260
Loading time in total (min)	31,500
2# stage driving gear loaded times in a single cycle	217,147
2# stage driving gear loaded times in the whole test	26,158,640

5. Conclusions

(1) The wheel-side electric drive system is supposed to be applied in different vehicle models. The traditional durability development for the certain kinds of vehicle load spectrum cannot meet the requirements of highly modularized development. To achieve highly efficient development with enough credibility, the comprehensive load spectrum is irreplaceable, while the modeling accuracy is decisive for the simulation and test.

(2) The electric motor drives the wheel through two-stage fixed axis helical gears, so the power transmission path is short and acts as the suspension arm at the same time. As a result, the gears are crucial to the system reliability and NVH performance. The gears are manufactured by the hobbing and form grinding process, which ensures high accuracy and supports a free-style tooth shaping modification. In the gear processing, the involute part and root fillet curve are generated by hobbing, and the final tooth shape is generated by grinding. Through geometric theory deduction, the relationship between the hob parameters and the tooth root fillet curve can be described functionally.

(3) Based on the rain flow methodology and extrapolation theory, a comprehensive load spectrum with nine stages is formulated, which can cover the working conditions of the basic version, NVH version, and durability version. According to the Miner cumulative damage hypothesis, the equivalent durability mileage of 150,000 km is converted. The prototype machine is simulated and verified on the test bench with the comprehensive load spectrum. The whole test lasts 525 h, with the estimated cumulative damage of the system to be 63.27%. The test result shows the robust performance of the system.

(4) The wheel-side electric drive system is applied in three models with different working conditions, which are the basic version, NVH version, and durability version. If tested in the traditional way, the bench test would take over 4500 h, which is totally unacceptable in terms of time cost and financial expense. The modularized development introduced in this paper takes 525 h, which significantly improves the test efficiency. And the modularized development can be even more efficient with more and more application models. The evaluation and conversion of different load spectra and the preciseness of teeth modeling play a vital role in the modularized development, which has been the main novelty of this paper.

(5) In the future, more work is needed regarding the technical trend in wire-by-chassis. The wheel-side electric drive system has the potential to be integrated and upgraded with the brake system and active suspension system. In this way, the actuators are all located near the wheel-end, which means they can offer a quick response in safety redundancies. This architecture is especially suitable for autonomous driving vehicles,

where the central controller is responsible for decision-making, and all the actuators at the wheel-end are responsible for rapid response. For the future application of wheel-side electric drive system, the research in this paper provides data support and a development reference for more applications in the future, including gear damage calculation, product lifespan evaluation, system reliability design, lightweight optimization, etc.

6. Patents

The work reported in this manuscript applied for a China patent in 2014. The patent is titled as "An integrated single trailing arm suspension with fixed axial gear reducer as a wheel-side electric drive system", with the patent number CN102745073B.

Author Contributions: Conceptualization, X.C. and X.D.; methodology, X.D. and W.W.; software, W.W.; validation, X.D. and W.W.; formal analysis, X.D.; investigation, X.D. and W.W.; resources, X.C. and X.D.; data curation, X.D. and W.W.; writing—original draft preparation, X.D.; writing—review and editing, X.C.; visualization, X.D.; supervision, X.C.; project administration, X.C.; funding acquisition, X.C. All authors have read and agreed to the published version of the manuscript.

Funding: This research was funded by the National Natural Science Foundation of China project "Research on the Mechanism Principle and Multi-source Information Processing Mechanism of a Load-sensing Distributed Drive System" (No. 5227052034).

Data Availability Statement: The data presented in this study are available on request from the corresponding author.

Conflicts of Interest: The author Xiaoyu Ding was employed by the company R&D Innovation Headquarters, SAIC Motor. The remaining authors declare that the research was conducted in the absence of any commercial or financial relationships that could be construed as potential conflicts of interest.

Abbreviations

The following abbreviations are used in this manuscript:

PMSM	Permanent magnet synchronous motor
NVH	Directory of open access journals
FEM	Finite element method
z	Tooth number
m	tooth modulus, mm
α	pressure angle, °
β	helix angle, °
h	addendum height coefficient
b	gear width, mm
d_b	base circle diameter, mm
d_p	pitch circle diameter, mm
a	center distance, mm
ε	coincidence
i	reduction ratio
r	corner radius of the blade
δ	the corner center of the blade to the center line of the hob
r	corner radius of the blade, mm
S	distance between the hob coordinate axis and the fixed coordinate axis, mm

References

1. Hori, Y. Future vehicle driven by electricity and control-research on four wheel motored "UOT Electric March II". *IEEE Trans. Ind. Electron.* **2004**, *51*, 954–962. [CrossRef]
2. Russell, H.E.B.; Gerdes, J.C. Design of variable vehicle handling characteristics using four-wheel steer-by-wire. *IEEE Trans. Control. Syst. Technol.* **2016**, *24*, 1529–1540. [CrossRef]
3. Sun, W.; Li, Y.; Huang, J.; Zhang, N. Vibration effect and control of In-Wheel switched reluctance motor for electric vehicle. *J. Sound Vib.* **2015**, *338*, 105–120. [CrossRef]
4. Chen, X.B.; Li, Y.; Yin, J.; Wang, C.; Ding, X.Y.; Yan, M.; Tang, F. An Integrated Single Trailing Arm Suspension with Fixed Axial Gear Reducer as a Wheel-Side Electric Drive System. Chinese Patent CN10274, 9 April 2014.
5. Chen, X.; Yin, J.; Wang, W.; Wu, L.; Tang, F. Approaches to diminish large unsprung mass negative effects of wheel side drive electric vehicles. *J. Adv. Mech. Des. Syst. Manuf.* **2016**, *10*, JAMDSM0064. [CrossRef]
6. Wang, W.; Chen, X.B. Design methodology for wheel corner module topology based on position and orientation characteristics. *Mech. Mach. Theory* **2019**, *136*, 122–140. [CrossRef]
7. Men, Y.Z.; Liu, B.; Li, M.D.; Yu, H.B.; Wang, S.Y.; Han, Y. A research on the load spectra development for reliability bench test of passenger car drive-train related to typical user data. *Automot. Eng.* **2017**, *39*, 1286–1293. [CrossRef]
8. Geng, S.; Liu, X.; Yang, X.; Meng, Z.; Wang, X.; Wang, Y. Load spectrum for automotive wheels hub based on mixed probability distribution model. *Proc. Inst. Mech. Eng. Part D J. Automob. Eng.* **2019**, *14*, 3707–3720. [CrossRef]
9. Wang, Z.; Zhao, L.; Kong, Z.; Yu, J.; Yan, C. Development of accelerated reliability test cycle for electric drive system based on vehicle operating data. *Eng. Fail. Anal.* **2022**, *141*, 106696. [CrossRef]
10. Facchinetti, M.L. Fatigue damage of materials and structures assessed by Wöhler and Gassner frameworks: Recent insights about load spectra for the automotive. *Procedia Eng.* **2018**, *213*, 117–125. [CrossRef]
11. Liu, X.; Tan, J.; Long, S. Multi-axis fatigue load spectrum editing for automotive components using generalized S-transform. *Int. J. Fatigue* **2024**, *188*, 108503. [CrossRef]
12. Buckingham, E. Surface fatigue of plastic materials: Progress report No. 16 of the ASME special research committee on strength of gear teeth. *Trans. Am. Soc. Mech. Eng.* **1944**, *66*, 297–306. [CrossRef]
13. Kawalec, A.; Wiktor, J.; Ceglarek, D. Comparative analysis of tooth-root strength using ISO and AGMA standards in spur and helical gears with FEM-based verification. *J. Mech. Des.* **2006**, *128*, 1141–1158. [CrossRef]
14. Chabert, G.; Tran, T.D.; Mathis, R. An evaluation of stresses and deflection of spur gear teeth under strain. *J. Manuf. Sci. Eng.* **1974**, *96*, 85–93. [CrossRef]
15. Spitas, V.; Spitas, C. Numerical and experimental comparative study of strength-optimised AGMA and FZG spur gears. *Acta Mech.* **2007**, *193*, 113–126. [CrossRef]
16. Oda, S.; Koide, T.; Ikeda, T.; Umezawa, K. Effects of pressure angle on tooth deflection and root stress. *JSME Int. J. Ser. B-Fluids Therm. Eng.* **1986**, *29*, 3141–3148. [CrossRef]
17. Bejar, F.; Perret-Liaudet, J.; Bareille, O.; Ichchou, M.; Fontana, M. Review and benchmarking study of different gear contact analysis software in terms of the static transmission error response. *Results Eng.* **2024**, *22*, 102286. [CrossRef]
18. Pedersen, N.L. Minimizing tooth bending stress in spur gears with simplified shapes of fillet and tool shape determination. *Eng. Optim.* **2015**, *47*, 805–824. [CrossRef]
19. Yi, J.; Jin, T.; Zhou, W.; Deng, Z. Theoretical and experimental analysis of temperature distribution during full tooth groove form grinding. *J. Manuf. Process.* **2020**, *58*, 101–115. [CrossRef]
20. Matsuo, K.; Suzuki, Y.; Hongu, J.; Iba, D.; Moriwaki, I. Method of designing gear-honing-wheel geometries (Considering of relative sliding velocities). *J. Adv. Mech. Des. Syst. Manuf.* **2021**, *15*, JAMDSM0010. [CrossRef]
21. Kruszyński, B.W.; Nawara, L. Model of gear-grinding process. *CIRP Ann. Manuf. Technol.* **1995**, *44*, 321–324. [CrossRef]
22. Gupta, K.; Jain, N.K.; Laubscher, R. *Advanced Gear Manufacturing and Finishing: Classical and Modern Processes*; Academic Press: New York, NY, USA, 2017; p. 18.
23. Manchoul, S.; Ben Sghaier, R.; Seddik, R.; Fathallah, R. Comparison between conventional shot peening and ultrasonic shot peening. *Mech. Ind.* **2018**, *19*, 603. [CrossRef]
24. Liang, X.; Liu, Z.; Wang, B.; Song, Q.; Cai, Y.; Wan, Y. Prediction of residual stress with multi-physics model for orthogonal cutting Ti-6Al-4V under various tool wear morphologies. *J. Mater. Process. Technol.* **2020**, *288*, 116908. [CrossRef]
25. Xia, C.; Wang, S.; Ma, C.; Wang, S.; Xiao, Y. Crucial geometric error compensation towards gear grinding accuracy enhancement based on simplified actual inverse kinematic model. *Int. J. Mech. Sci.* **2020**, *169*, 105319. [CrossRef]
26. Hsieh, J.K.; Tseng, H.C.; Chang, S.L. A novel hob cutter design for the manufacture of spur-typed cutters. *J. Mater. Process. Technol.* **2009**, *209*, 847–855. [CrossRef]
27. Zhang, Z. *Failure and Countermeasures of Gear Transmission*; China Machine Press: Beijing, China, 2011; pp. 77–85. (In Chinese)
28. Krol, O.; Sokolov, V. *Parametric Modeling of Gear Cutting Tools*; Springer: Berlin/Heidelberg, Germany, 2019. [CrossRef]

29. Deng, S.C.; Zhao, L.H.; Wang, Z.; Zhou, C.; Zheng, S.L. A Method of Rapid Construction of Reliability Target Load for Electric Drive Systems. *Chin. J. Automot. Eng.* **2021**, *11*. (In Chinese) [CrossRef]
30. Zheng, S.L.; Wang, S.; Feng, J.; Chen, T.; Yu, J.W. Durability test of hub reducer system based on low load strengthening. *J. Univ. Shanghai Sci. Technol.* **2016**, *38*, 1. (In Chinese)
31. Yu, W.Y.; Zheng, S.L.; Feng, J.Z.; Wang, Z.; Guo, Z.X. A study on the design principle of load spectra for the shafting parts in wheel hub reducer of electric vehicle. *Automot. Eng.* **2018**, *40*, 1. (In Chinese) [CrossRef]
32. Zhao, L.H.; Zheng, S.L.; Feng, J.Z. Failure mode analysis of torsion beam rear suspension under service conditions. *Eng. Fail. Anal.* **2014**, *36*, 39–48. [CrossRef]
33. Wang, B.; Chen, X.; Lyu, H.M.; Niu, X.W. Study on wheel-side drive system with a single trailing arm. *Int. J. Automot. Technol.* **2021**, *22*, 1215–1226. [CrossRef]

Disclaimer/Publisher's Note: The statements, opinions and data contained in all publications are solely those of the individual author(s) and contributor(s) and not of MDPI and/or the editor(s). MDPI and/or the editor(s) disclaim responsibility for any injury to people or property resulting from any ideas, methods, instructions or products referred to in the content.